

Spectroscopy of a cold strontium Rydberg gas

J. Millen, G. Lothead, G. R. Corbett, R. M. Potvliege and M. P. A. Jones*

Department of Physics, Durham University, Durham DH1 3LE, United Kingdom

(Dated: October 25, 2018)

We present a study of a cold strontium Rydberg gas. The narrowband laser excitation of Rydberg states in the range $n = 20 - 80$ from a 6 mK cloud of strontium atoms is detected using the spontaneous ionization of the Rydberg atoms. Using a high-resolution step-scanning technique, we perform detailed measurements of the Stark maps of selected Rydberg states. We find excellent agreement between the measured Stark maps and a numerical calculation based on an independent-electron model. Finally we show that excitation of the second valence electron can be used to probe the dynamics of the Rydberg gas with nanosecond temporal resolution via autoionization.

INTRODUCTION

Rydberg atoms offer an ideal opportunity to study strongly interacting quantum systems, due to the long-range dipole-dipole interactions between them. Two individually trapped neutral atoms excited to Rydberg states have been shown to exhibit a high degree of entanglement, through the dipole blockade mechanism [1–4]. These entangled states are important for the study of quantum information, as they can be used to perform quantum gate operations [5]. In mesoscopic atom clouds, the dipole blockade effect leads to the formation of highly-correlated many-body states [6] that can exhibit long-range crystalline order [7, 8]. The dipole blockade also modifies the atom-light interactions [9], giving rise to cooperative optical effects [10] which could be exploited to create photonic phase gates [11]. The long-range interactions cause Rydberg gases to spontaneously evolve into cold neutral plasmas [12] through spontaneous ionization.

Most experiments in this field have used alkali metal atoms, where only a single valence electron is available for manipulation. Divalent atoms, such as strontium, open up new opportunities for the study of Rydberg gases. For Rydberg states of low angular momentum L , excitation of the inner valence electron leads to autoionization, which can be used as a state-selective probe of the interactions in a cold Rydberg gas [13]. Off resonance, the strong optical transitions of the ionic core can be exploited to create optical dipole traps for Rydberg atoms [14]. For states of high L the inner valence electron can be excited without ionizing the atom [15], raising the possibility of imaging the Rydberg atoms, in a similar manner to the direct imaging of Sr^+ ions in a cold plasma [16].

In this paper we discuss the creation and manipulation of a cold strontium Rydberg gas. We describe the cold Rydberg gas apparatus (section I), and present a high-resolution spectroscopic study of selected Rydberg states at principal quantum number $n > 50$ (section II). In order to understand the behaviour of cold Rydberg gases, a clear understanding of the nature of the dipole-dipole

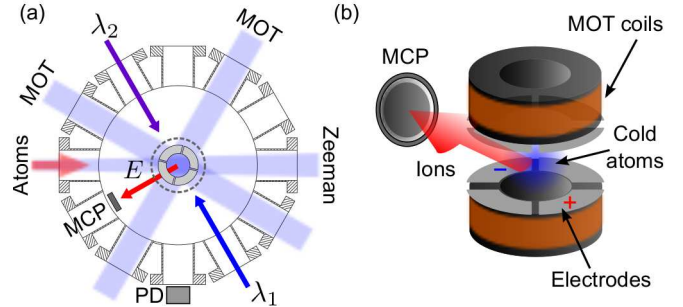


FIG. 1. (a) A scale diagram of the vacuum chamber. Zeeman-slowed atoms enter from the left. Electrodes create an electric field E that directs ions to the MCP. The fluorescence from the MOT is monitored by a photodiode (PD). The Rydberg excitation beams λ_1 and λ_2 (see figure 2(a)) are also shown. (b) A schematic of the apparatus inside the vacuum chamber. The MOT coils are wound on copper formers, which also support eight electrodes in a split-ring geometry.

interactions is essential. This requires a knowledge of the dipole matrix elements. We present a detailed numerical calculation of the Stark maps based on dipole matrix elements calculated using an independent electron model, and find very good quantitative agreement with experiment (section III). Finally we show that laser excitation of the second valence electron can be used as a high time-resolution probe of the Rydberg gas (section IV)

I. EXPERIMENTAL SET-UP

Cold ^{88}Sr atoms are prepared in a standard six-beam magneto-optical trap (MOT) operating on the $5s^2\ ^1S_0 \rightarrow 5s5p\ ^1P_1$ transition at 461 nm. This light is produced by a frequency doubled diode laser system (Toptica TA-SHG). To stabilize the laser at 461 nm, we perform polarization spectroscopy [17] in a strontium dispenser cell [18]. A schematic of the trapping region is shown in figure 1(a). A MOT for strontium requires a magnetic field gradient of $\sim 30\text{ G cm}^{-1}$. The field coils are mounted inside the vacuum system, so that this field can be produced without the need for water cooling. The coils are made from Kapton insulated copper wire wound onto copper

* m.p.a.jones@durham.ac.uk

formers.

A micro-channel plate (MCP) detector is mounted inside the vacuum system to detect ions produced in the Rydberg gas. The MCP is positioned away from the line of-sight of the atomic beam, as shown on figure 1(a), and is further protected by a baffle. A wire mesh grid electrode placed in front of the MCP is used to control the stray electric field from the detector. The grid is typically held at -10 V. An additional electric field is used to direct ions to the MCP. The field is created by eight independently controllable electrodes, arranged in a split-ring geometry [19]. The electrodes are mounted onto the MOT coil formers, as shown in figure 1(b), and insulated from the copper with ceramic spacers.

The trap is loaded from a Zeeman slowed atomic beam. Strontium is heated in an oven, which consists of heater wire wrapped around the outside of a standard stainless steel vacuum tube [20]. The hot strontium is collimated using a bundle of 8 mm long, $170 \mu\text{m}$ diameter steel capillaries, held in a nozzle which is separately heated to prevent condensation of the strontium. The hot atomic beam passes through a 30 cm long solenoid-type Zeeman slower. The Zeeman slower is encased in a mild steel yoke to boost the magnetic field at the ends of the slower, and further shield the trapped atoms from stray magnetic fields. We typically trap 4×10^6 atoms, at a density of $2 \times 10^{10} \text{ cm}^{-3}$ and a temperature of 6 mK.

The Rydberg sample is prepared using a two-step excitation $\lambda_1 + \lambda_2$, as illustrated in figure 2(a). The light for the first step, $\lambda_1 = 461 \text{ nm}$, is derived from the cooling laser, and is resonant with the $5s^2^1S_0 \rightarrow 5s5p^1P_1$ transition. The light for the second step (the Rydberg excitation), λ_2 , is produced by one of two frequency doubled diode laser systems (Toptica DLS SHG), at 420 nm or 413 nm, depending on the range of Rydberg states we wish to access. Both beams are pulsed on simultaneously for $4 \mu\text{s}$. The beams are overlapped, counter-propagating, and linearly polarized in the vertical direction. They propagate normal to the direction of the electric field at the position of the cold atoms.

The wavelength of the fundamental of the Rydberg excitation laser is measured using a High Finesse WS7 wavemeter, and is converted into the output laser frequency ω_2 .

The next section outlines a method for performing Rydberg state spectroscopy using this experimental set-up.

II. HIGH RESOLUTION RYDBERG SPECTROSCOPY

We perform spectroscopy by varying the frequency ω_2 of the Rydberg excitation laser, and measuring the amount of spontaneous ionization. Spontaneous ionization has been observed in nearly all experiments on cold Rydberg gases. The dominant mechanism is thought to be interaction-enhanced Penning ionization [21, 22]. In our experiment ionization could also arise from collisions

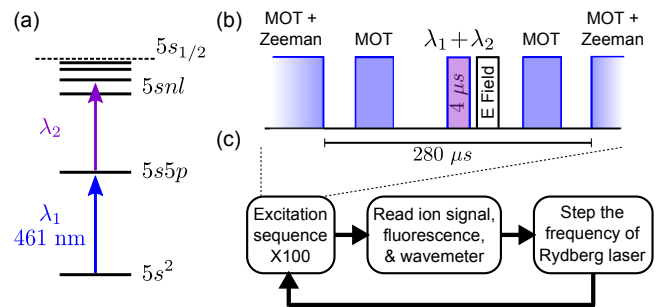


FIG. 2. (a) Energy level diagram for the two-step excitation, $\lambda_1 + \lambda_2$, to a Rydberg state $5snl$. (b) Timing diagram for the excitation sequence. The Rydberg state is populated after the ground-state atoms are released from the MOT. The MOT light is pulsed before and after the Rydberg excitation. (c) Experimental sequence for the step-scan technique. The Rydberg excitation sequence is repeated 100 times. The averaged ion signal and fluorescence, and the frequency ω_2 of λ_2 , are recorded. The frequency ω_2 is stepped, and the process repeated to produce a spectrum.

with hot atoms not captured by the Zeeman slower [12]. We observe ionization for all of the states we have studied, which include states of principal quantum number $n = 18$ and above. The ionization is present regardless of whether the interatomic interactions are attractive (as is the case for the 1S_0 states in Sr [14]), or repulsive (as is the case for the 1D_2 states above $n = 25$). The ionization is rapid [23]; we observe ionization within $1 \mu\text{s}$ of starting the Rydberg excitation. At the Rydberg densities used in this paper ($< 5 \times 10^8 \text{ cm}^{-3}$), the spontaneous ionization signal is proportional to the Rydberg excitation laser intensity. At higher Rydberg densities we observe the formation of a cold plasma [13], which leads to avalanche ionization [12].

The spontaneously created ions are directed to the MCP with a $4 \mu\text{s}$ long electric field pulse. The amplitude of this pulse (4 V cm^{-1}) is not sufficient to field ionize any of the Rydberg states described in this paper. The signal from the MCP is amplified, recorded on a digital oscilloscope and integrated to yield a total ion signal in $\text{V } \mu\text{s}$.

The sequence that we use to perform spectroscopy is illustrated in figure 2(b). A pulse of MOT light before and after the Rydberg excitation is used to measure the ground state atom number and any loss of atoms. This excitation sequence is repeated 100 times, and the ionization and fluorescence signals are averaged on the oscilloscope. After the 100 repeats the average signals are recorded, and the frequency ω_2 is sampled 100 times. A voltage is applied to the laser piezo to step the frequency ω_2 , and whole process is repeated, as illustrated in figure 2(c). By repeatedly stepping ω_2 we can build up a Rydberg state spectrum. We refer to this method as the “step-scan” technique. The entire stepping and recording process is automated under computer control.

Importantly, measuring ω_2 at each step enables us to

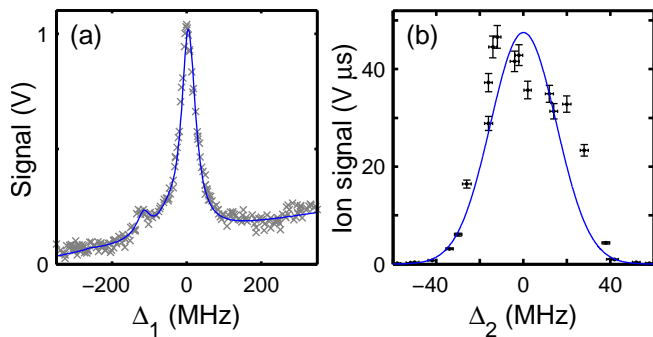


FIG. 3. Example spectra obtained using the step-scan technique. The detunings Δ_1, Δ_2 are defined relative to our measured line centres. (a) Saturated absorption spectrum of the $5s^2\ ^1S_0 \rightarrow 5s5p\ ^1P_1$ transition. The fit is a sum of six Lorentzians. (b) Spectrum of the $5s19d\ ^1D_2$ state. The solid line is a Gaussian fit with a FWHM of 48 MHz, which matches the linewidth of the $5s5p\ ^1P_1$ state (32 MHz) with expected power-broadening.

negate the effect of slow drifts in the laser frequency. To characterize the accuracy of this step-scan technique, we performed saturated absorption spectroscopy of the $5s^2\ ^1S_0 \rightarrow 5s5p\ ^1P_1$ transition, as shown in figure 3(a). The frequency ω_1 of the 461 nm laser is stepped across the resonance in steps of 1.4 MHz, which are clearly resolved by the wavemeter. We fit the spectrum with a sum of six Lorentzians, one for each isotope and hyperfine component [24]. The free parameters are the overall amplitude, a sloping background and a frequency axis scaling parameter α , such that $\omega_1 \rightarrow \alpha\omega_1$. From the fit, we obtain $\alpha = 1.03 \pm 0.02$, indicating that the relative frequency accuracy is very good. By comparing our measured wavelengths to literature values, we estimate that the absolute accuracy of the wavemeter is ~ 200 MHz. This is consistent with the wavemeter specification when using multi-mode optical fibres.

Examples of the Rydberg spectra that we obtain are shown in figures 3(b) and 4. Figure 3(b) shows a high-resolution scan across a single Rydberg state. The linewidth of the Rydberg excitation is consistent with the power-broadened linewidth of the intermediate $5s5p\ ^1P_1$ state. In figure 4 the Rydberg laser is stepped over 8 GHz, in steps of 7 MHz, in the vicinity of the $5s80d\ ^1D_2$ state. This spectrum was acquired in the presence of a constant electric field of $0.35\ \text{V cm}^{-1}$, which allows the excitation of the dipole-forbidden 1P_1 state. Triplet states are also visible in the spectrum, indicating that singlet-triplet mixing [25] is still present even at $n = 80$. The $81\ ^3S_1$ peak is ~ 200 times smaller than the principal $80\ ^1D_2$ peak, which highlights that spontaneous ionization is detectable even for these extremely weakly populated states.

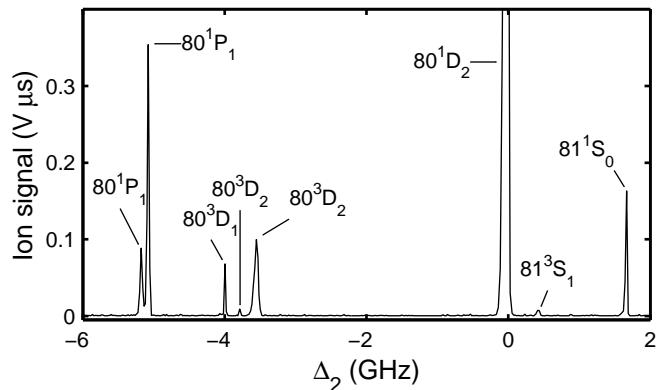


FIG. 4. Spectrum in the region $n = 80$, in the presence of a $0.35\ \text{V cm}^{-1}$ electric field. The detuning Δ_2 is relative to the energy of the $80\ ^1D_2$ state in zero field. The $80\ ^1D_2$ state signal peaks at $1.4\ \text{V } \mu\text{s}$. The electric field allows otherwise forbidden transitions, and has split the $80\ ^1P_1$ and $80\ ^3D_2$ states into their $|m_J\rangle$ components. The lines are assigned using the single electron simulation.

III. SINGLE ELECTRON MODEL AND STARK MAPS

Rydberg atoms exhibit greatly enhanced interatomic interactions as compared to ground state atoms. To calculate the size and form of these interactions the dipole matrix elements between different atomic states must be known. This requires a knowledge of the atomic state wavefunctions. For the alkali elements, the wavefunctions are commonly calculated by considering a single electron moving in a model potential, which incorporates the effect of the valence electron penetrating the closed electronic shells [26].

The situation for alkali earth elements is more complex, since there are two valence electrons. This leads to perturbations in the energy level structure due to the presence of doubly excited perturber states [27]. To fully describe the energy level structure of the alkali earth elements, multi-channel quantum defect theory (MQDT) must be used [28]. However, [29] recently obtained good agreement between experimental and theoretical Sr Stark maps in the region of principal quantum number $n = 12$, using dipole matrix elements obtained by treating the two electrons as completely independent and moving in a simple model potential. In the following, we extend this model to much higher values of n and total orbital angular momentum L , and find that it remains in good agreement with our experimentally measured Stark maps.

Our simulation uses known quantum defects [25, 30, 31], and extrapolates them to regions where they have not been previously measured. Using these values we fit a model potential of the Klapisch form [32] using a simulated annealing algorithm. Radial wavefunctions are calculated, using the Numerov method [33], by considering a single electron moving in this model potential. Dipole matrix elements are calculated from the radial wavefunc-

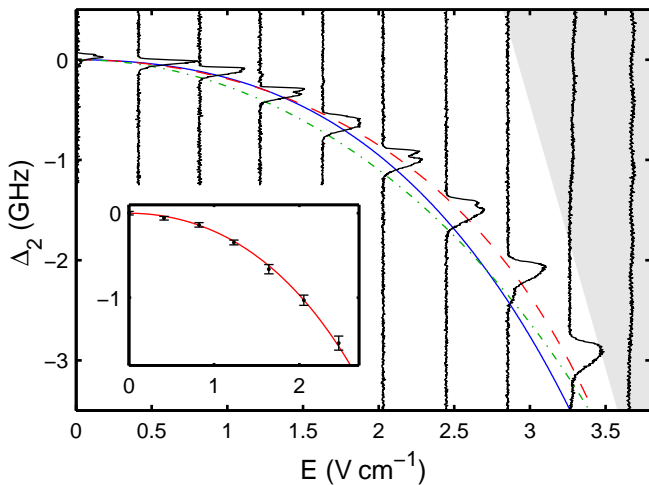


FIG. 5. Stark map in the region of the $5s56d\ ^1D_2$ state. The detuning Δ_2 is relative to the energy of the state in zero electric field. The blue (solid), red (dashed), green (dot-dashed) lines are the simulated $|m_J| = 0, 1, 2$ components respectively. The grey region is the high angular momentum manifold. The inset shows the fit of the simulated Stark shift averaged over the three $|m_J|$ components (red line) to the experimental centre frequency (black dots), extracted using a Gaussian fit to the lineshape at each electric field. The linewidth (FWHM) is indicated by the error bars.

tions [34]. To calculate a Stark map in the region $n = n_0$ states of $n = n_0 \pm 5$ are included, and the angular momentum L states are truncated at $L = 40$.

The Stark map is measured using the step-scan technique, with a static electric field applied during the Rydberg excitation. Measured and simulated Stark maps are shown in the region of the $5s56d\ ^1D_2$ state in figure 5, and the $5s80d\ ^1D_2$ in figure 6. In order to compare experiment and theory, the calibration factor between the applied voltage and the electric field must be determined. The calibration factor is obtained by fitting the simulated Stark map to the experimental data, as shown in the inset to figure 5. There are three fitting parameters: the calibration factor, the voltage offset due to the stray electric field, and a frequency offset due to the wavemeter uncertainty. We constrain the voltage offset using the variation in the amplitude of the $80\ ^1P_1$ peak with electric field. This state cannot be populated in zero field, since we excite via the $5s5p\ ^1P_1$ state. The fit shown in the inset to figure 5 yields a calibration factor of $0.205 \pm 0.005\ \text{V cm}^{-1}$ per volt applied. A similar fit to the $n = 80$ Stark map yields a calibration factor of $0.215 \pm 0.005\ \text{V cm}^{-1}$ per volt applied. The corresponding value for the stray electric field obtained from the voltage offset is $2.8 \pm 0.4\ \text{mV cm}^{-1}$. This is consistent with the estimated electric field due to the MCP grid.

These calibration curves highlight the excellent quantitative agreement between the single electron model and the experiment for the 1D_2 states. In figure 5(a), the splitting between the $|m_J| = 0, 1, 2$ (blue solid, red

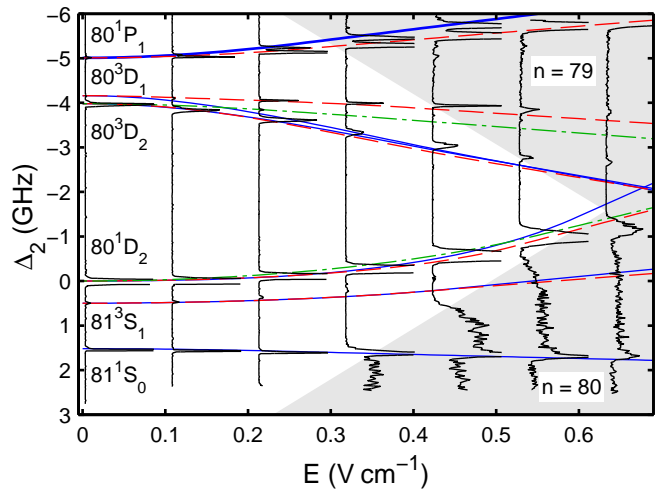


FIG. 6. A Stark map in the region of the $5s80d\ ^1D_2$ state. Solid black lines are the experimental spectra. The detuning Δ_2 is relative to the energy of the $80\ ^1D_2$ state in zero electric field. The blue (solid), red (dashed), green (dot-dashed) lines are the simulated $|m_J| = 0, 1, 2$ components respectively, and the grey shaded areas represent the simulated high angular momentum manifolds. The $80\ ^3D_3$ state is doubly forbidden and is not observed.

dashed, green dot-dashed lines) agree well with the data (black lines), and the interaction with the higher angular momentum manifold (grey region) is correctly predicted and visible in the data. The agreement is also very good across the $n = 80$ Stark map shown in figure 6. The only previously measured state energy in this region is for the $5s80d\ ^1D_2$ state [30], and we have adjusted the quantum defects for the other series to match our measured splitting from the $80\ ^1D_2$ state in zero field. This requires a change of $< 1\%$ from the extrapolated quantum defects. The interaction of the low L states with the high angular momentum manifolds (shaded grey areas on figure 6) is clearly visible. The agreement is better for the singlet states than the triplet states. More quantum defects must be found by extrapolation for the triplet series, as the spectroscopic data is less complete. Alternatively, the disagreement may reflect the fact that the single electron model ignores the mixing between the singlet and triplet states.

We have shown that a single electron model can be used to calculate dipole matrix elements for strontium, over a large range of n . The single electron model is therefore appropriate for calculating the dipole-dipole interactions, which depend on these matrix elements [14]. The single electron model does not work for predicting state lifetimes and line strengths, which are strongly perturbed by the presence of doubly excited states. To fully describe the energy level structure of the alkali earth elements multi-channel quantum defect theory (MQDT) must be used [28], which takes into account the divalent nature of the atom.

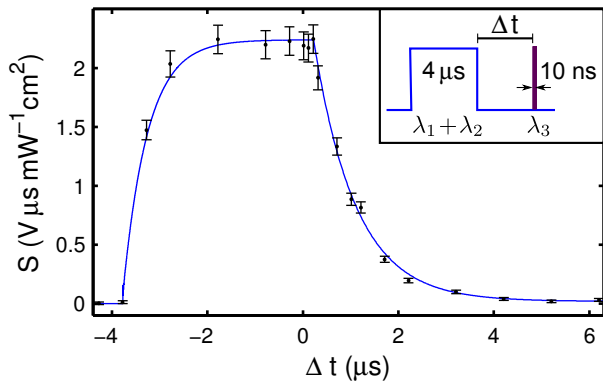


FIG. 7. The autoionization signal for the $5s19d\ ^1D_2$ state as a function of time. $\Delta t = 0$ is defined as the end of the $4\ \mu\text{s}$ long excitation to the Rydberg state $\lambda_1 + \lambda_2$, as illustrated in the inset. The solid line is the solution to the optical Bloch equations.

IV. PULSED AUTOIONIZATION

Rather than relying on spontaneous ionization, we can detect the Rydberg atoms using autoionization by exciting the inner valence electron. If an atom is initially prepared in a Rydberg state, the inner valence electron can be excited independently, a process known as isolated core excitation [35]. The doubly excited states couple not only to each other (as with singly excited states), but also to the degenerate continuum. For states of low angular momentum L this leads to rapid ionization, and these states are referred to as “autoionizing”. There has been much research into the nature of autoionizing resonances, with MQDT proving to be extremely powerful for describing doubly excited states [28]. The autoionization process has a large cross-section, and hence produces significantly more ions than spontaneous ionization. We typically find that by exciting an autoionizing resonance the signal is increased by a factor of 100.

We prepare atoms in the $5snl$ Rydberg state, using the same sequence as before (figure 2). At a variable time Δt after the end of the excitation to the Rydberg state, a $10\ \text{ns}$ light pulse at $\lambda_3 = 408\ \text{nm}$ excites the inner valence electron, creating the autoionizing state $5p_{3/2}n'l$. The light λ_3 is provided by a tunable pulsed dye laser system, with a bandwidth of a few GHz, and a repetition rate of $10\ \text{Hz}$. The autoionizing pulse is immediately followed by an electric field pulse that directs the ions to the MCP.

At each value of the wavelength λ_3 and delay Δt we measure a Rydberg spectrum using the step-scan technique described previously. The spectrum is normalized by the average pulse intensity measured on a photodiode, and the ground state atom number. From this spectrum we extract the peak autoionization-enhanced ion signal, S , in units of $\text{V}\ \mu\text{s}\ \mu\text{W}^{-1}\ \text{cm}^2$ per 10^6 atoms.

By fixing the wavelength λ_3 and scanning the delay Δt across the $4\ \mu\text{s}$ Rydberg excitation pulse, the evolution of

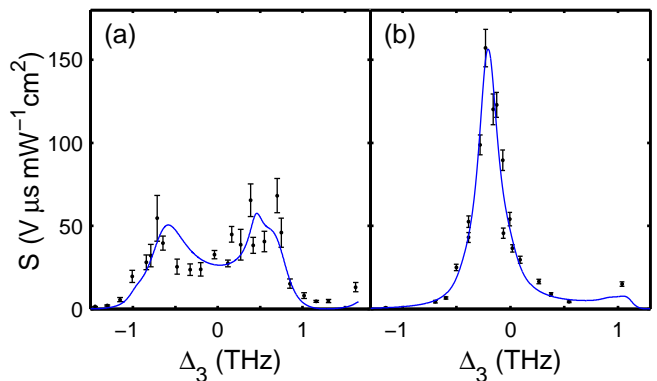


FIG. 8. Autoionization spectra of the (a) $5s19d\ ^1D_2$ and (b) $5s20s\ ^1S_0$ states. The spectra are fit with a six-channel MQDT model. Δ_3 is the detuning of ω_3 from the $5s_{1/2} \rightarrow 5p_{3/2}$ ion transition. These spectra are taken at a delay $\Delta t = 0.5\ \mu\text{s}$.

the Rydberg population can be mapped with high time resolution as shown in figure 7. Both the Rydberg excitation and subsequent decay are clearly visible. By fitting an exponential to the decay we find a state lifetime of $\tau_{19D} = 880 \pm 30\ \text{ns}$. The complete time evolution can be modelled by solving the three level optical Bloch equations for the scheme $5s^2\ ^1S_0 \rightarrow 5s5p\ ^1P_1 \rightarrow 5s19d\ ^1D_2$. The Rabi frequencies and decay constants for each step of the excitation are constrained using our measurements of the laser intensity and the lifetime τ_{19D} , and the oscillator strength for the $5s5p\ ^1P_1 \rightarrow 5s19d\ ^1D_2$ transition from [36]. The only remaining free parameter is the amplitude scale. The fit is in very good agreement with the data, as can be seen in figure 7. This indicates that the autoionization signal is proportional to the Rydberg state population. An identical analysis for the $5s20s\ ^1S_0$ state yields a state lifetime of $3.1 \pm 0.1\ \mu\text{s}$.

By fixing the delay Δt , and varying the wavelength λ_3 , the spectrum of the $5snl \rightarrow 5p_{3/2}n'l$ autoionizing transition can be measured. MQDT allows us to reproduce the spectra of the autoionizing states, which in turn allows us to identify exactly which state a sample is in from its autoionization spectrum. The spectra are fit with a six-channel MQDT model, using the same fitting parameters as [37] for the $19\ ^1D_2$ state (with the elliptical polarization of λ_3 included in the model), and [38] for the $20\ ^1S_0$ state. The difference in the shape of the spectra is due to the difference $\epsilon = \delta_b - \delta_a$ between the bound (Rydberg) state quantum defect δ_b , and the autoionizing state quantum defect δ_a . For $\epsilon \simeq 0$ (modulo-one) each Rydberg state only overlaps with a single autoionizing state, and the autoionizing spectrum is a single peak, as seen for the $20\ ^1S_0$ state with $\epsilon = 0.15$. For $\epsilon \simeq 0.5$ (modulo-one) each Rydberg state overlaps with two autoionizing states, and the autoionizing spectrum is double-peaked, as seen for the $19\ ^1D_2$ state with $\epsilon = 0.46$.

The spectra in figure 8 illustrate that autoionization can be used for state-selective detection. It is particularly sensitive to changes in L . In previous work we have

identified, and quantified, transfer of population from one Rydberg state to another through analysis of the autoionization spectra [13]. In the region $n \approx 20$ the autoionization spectra are approximately 1 THz wide as shown in figure 8. Even at $n = 56$, the width of the autoionizing spectrum for low- L states is > 10 GHz [13]. The high temporal resolution of the autoionization technique displayed in figure 7 can therefore be fully exploited without compromising its state-selectivity. The combination of high temporal resolution, state-selectivity and large signal-to-noise ratio make autoionization a powerful technique for probing the dynamics of cold Rydberg gases.

CONCLUSION

The use of alkali earth elements such as strontium offer new ways to study and manipulate Rydberg atoms. We have performed the first study of Rydberg states in a

cold gas of strontium. We have used, and experimentally verified, a simple single-electron model to find dipole matrix elements, which can be used to calculate interatomic interaction strengths. We have also used autoionization through two-electron excitation as a high-yield probe of a cold Rydberg gas, which can measure state population dynamics with high temporal resolution. By focusing the autoionizing laser this technique could be used to spatially probe the Rydberg gas, on length scales comparable to the dipole blockade radius.

We thank J.D. Pritchard for assistance with the dipole matrix element calculations, and C. S. Adams and D. Carty for the loan of equipment. This work was supported by EPSRC Grants No. EP/D070287/1 and No. LP/82000, and by Durham University.

BIBLIOGRAPHY

-
- [1] Lukin M D, Fleischhauer M and Cote R 2001 *Phys. Rev. Lett.* **87** 037901
- [2] Urban E, Johnson T A, Henage T, Isenhower L, Yavuz D D, Walker T G and Saffman M 2009 *Nature Physics* **5** 110–114
- [3] Gaëtan A, Miroshnychenko Y, Wilk T, Chotia A, Viteau M, Comparat D, Pillet P, Browaeys A and Grangier P 2009 *Nature Physics* **5** 115–118
- [4] Heidemann R, Raitzsch U, Bendkowsky V, Bütscher B, Löw R, Santos L and Pfau T 2007 *Phys. Rev. Lett.* **99** 163601
- [5] Saffman M, Walker T G and Mølmer K 2010 *Rev. Mod. Phys.* **82** 2313–2363
- [6] Weimer H, Löw R, Pfau T and Büchler H P 2008 *Phys. Rev. Lett.* **101** 250601
- [7] Pohl T, Demler E and Lukin M D 2010 *Phys. Rev. Lett.* **104** 043002
- [8] Schachenmayer J, Lesanovsky I, Micheli A and Daley A J 2010 *New J. Phys.* **12** 103044
- [9] Schempp H, Günter G, Hofmann C S, Giese C, Saliba S D, DePaola B D, Amthor T and Weidemüller M 2010 *Phys. Rev. Lett.* **104** 173602
- [10] Pritchard J D, Maxwell D, Gauguet A, Weatherill K J, Jones M P A and Adams C S 2010 *Phys. Rev. Lett.* **105** 193603
- [11] Friedler I, Petrosyan D, Fleischhauer M and Kurizki G 2005 *Phys. Rev. A* **72** 043803
- [12] Robinson M P, Laburthe Tolra B, Noel M W, Gallagher T F, Pillet P 2000 *Phys. Rev. Lett.* **85** 4466–4469
- [13] Millen J, Lothead G and Jones M P A 2010 *Phys. Rev. Lett.* **105** 213004
- [14] Mukherjee R, Millen J, Nath R, Jones M P A and Pohl T *J. Phys. B: At. Mol. Opt. Phys.* ? ?
- [15] Jones R R, Dai C J and Gallagher T F 1990 *Phys. Rev. A* **41** 316–326
- [16] Simien C E, Chen Y C, Gupta P, Laha S, Martinez Y N, Mickelson P G, Nagel S B and Killian T C 2004 *Phys. Rev. Lett.* **92** 143001
- [17] Javaux C, Hughes I G, Lothead G, Millen J and Jones M P A 2010 *Eur. Phys. J. D* **57** 151–154
- [18] Bridge E M, Millen J, Adams C S and Jones M P A 2009 *Rev. Sci. Instr.* **80** 013101
- [19] Löw R, Raitzsch U, Heidemann R, Bendkowsky V, Bütscher B, Grabowski A and Pfau T 2007 *Preprint quant-ph/0706.2639*
- [20] Courtillot I, Quessada A, Kovacich R P, Zondy J-J, Landragin A, Clairon A and Lemonde P 2003 *Optics Letters* **28** 468–470
- [21] Li W, Tanner P J and Gallagher T F 2005 *Phys. Rev. Lett.* **94** 173001
- [22] Amthor T, Denskat J, Giese C, Bezuglov N N, Ekers A, Cederbaum L S and Weidemüller M 2009 *Eur. Phys. J. D* **53** 329–335
- [23] Amthor T, Reetz-Lamour M, Westermann S, Denskat and Weidemüller M 2007 *Phys. Rev. Lett.* **98** 023004
- [24] Mauger S, Millen J and Jones M P A 2007 *J. Phys. B: At. Mol. Opt. Phys.* **40** F319–325
- [25] Esherick P 1977 *Phys. Rev. A* **15** 1920–1936
- [26] Theodosiou C E 1984 *Phys. Rev. A* **230** 2881–2909
- [27] Gallagher T F 1994 *Rydberg Atoms* (Cambridge University Press)
- [28] Aymar M, Greene C H and Luc-Koenig E 1996 *Rev. Mod. Phys.* **68** 1015–1123
- [29] Zhi M C, Dai C J and Li S B 2001 *Chinese Physics* **10** 929–934
- [30] Beigang R, Lücke K, Timmermann A, West P J and Frölich D 1982 *Opt. Commun.* **42** 19–24
- [31] Moore C E 1952 *Atomic Energy Levels (Chromium Through Niobium)* (US government printing office, Washington) Vol. 2; Garton W R S and Codling K 1968 *J. Phys. B: At. Mol. Opt. Phys.* **1** 106–113; Rubbmark J R and Borgström S A 1978 *Physica Scripta* **18** 196–208; Armstrong J A, Wynne J J and Esherick P 1979 *J. Opt. Soc. Am.* **69** 211–230;

- Beigang R, Lücke K, Schmidt D, Timmermann A and West P J 1982 *Physica Scripta* **26** 183–188;
Beigang R and Schmidt D 1983 *Physica Scripta* **27** 172–174;
Dai C J 1995 *Phys. Rev. A* **52** 4416–4424
- [32] Klapisch M 1971 *Comput. Phys. Comm.* **2** 239–260
[33] Hajj F Y 1980 *J. Phys. B: At. Mol. Opt. Phys.* **13** 4521–4528
[34] Potvliege R M 1998 *Comput. Phys. Comm.* **114** 42–93
[35] Cooke W E, Gallagher T F, Edelstein S A and Hill R M 1978 *Phys. Rev. Lett.* **40** 178–181
[36] Haq S-U, Mahmood S, Kalyar M A, Rafiq M, Ali R and Baig M A 2007 *Eur. Phys. J. D* **44** 439–447
[37] Xu E Y, Zhu Y, Mullins O C and Gallagher T F 1987 *Phys. Rev. A* **35** 1138–1148
[38] Xu E Y, Zhu Y, Mullins O C and Gallagher T F 1986 *Phys. Rev. A* **33** 2401–2409